Mechanical Systems and Signal Processing 114 (2019) 539–555

Contents lists available at ScienceDirect

Mechanical Systems and Signal Processing

journal homepage: www.elsevier.com/locate/ymssp

Restoration of low-informative image for robust debris shape measurement in on-line wear debris monitoring

Hongkun Wu [a,*], Ruowei Li [a], Ngai Ming Kwok [a], Yeping Peng [b], Tonghai Wu [c], Zhongxiao Peng [a]

[a] *School of Mechanical and Manufacturing Engineering, The University of New South Wales, Sydney, NSW 2032, Australia*
[b] *Shenzhen Key Laboratory of Electromagnetic Control, Shenzhen University, Shenzhen 518060, China*
[c] *Key Laboratory of Education Ministry for Modern Design and Rotor Bearing System, Xi'an Jiaotong University, Xi'an 710049, China*

ARTICLE INFO

Article history:
Received 5 December 2017
Received in revised form 23 February 2018
Accepted 16 May 2018
Available online 25 May 2018

Keywords:
Wear debris
Machine condition monitoring
Image restoration
Image fusion
Three dimensional measurement

ABSTRACT

As a significant technique in machine condition monitoring, wear debris analysis enables investigation of machine running condition with respect to debris features including size, quantity and morphology. In particular, being capable of providing more comprehensive morphological information, three-dimensional debris features are regarded essential and often acquired through a video-based debris imaging process. However, debris images captured often suffer degradation due to debris motion blur and lubrication contamination, that hinder reliable debris features extraction. To address the image degradation issue, a new method of wear debris image restoration is developed to reduce the effect of blur. In order to avoid the expensive computation involved in blind deconvolution methods, the debris image was restored using localized boundary features. Based on the fact that debris area and background area indicate distinctive brightness, a step edge model is applied to describe the original debris boundary. Localized kernels on each side of debris are then determined. Next, restorations are conducted with the estimated kernels to produce sharper debris profiles with respect to different motion features. Final restoration is conducted by fusing the restored profiles according to the maximum local sharpness. Experimental results have demonstrated that this method allows reliable features extraction from blurred image, improving the robustness of video based wear debris analysis.

1. Introduction

Condition monitoring of machinery is widely used to evaluate machine operation status so that proper maintenance can be scheduled to postpone or avoid catastrophic failure. Among the existing condition monitoring strategies, wear debris analysis has been recognized as a highly effective one [1]. By inspecting debris characteristics including quantity, size and morphology, wear status of mechanical components can be estimated [2–5]. To obtain comprehensive debris features, in particular, for wear mechanism assessment, image-oriented debris monitoring such as ferrography was developed [6]. However, those traditional approaches are being challenged recently, due to demands for rapid data interpretation in modern condition monitoring [7]. Consequently, sensing approaches had been redirected towards on-line wear debris image acquisition and analysis.

* Corresponding author.
E-mail address: hongkun.wu@unsw.edu.au (H. Wu).

https://doi.org/10.1016/j.ymssp.2018.05.032
0888-3270/

Over the past decades, various image based on-line wear debris analysis methods have been developed to conduct real-time debris data acquisition and interpretation [8]. Implementation of those sensing techniques proved that on-line approaches provide data more efficiently, and making it possible to schedule more timely maintenance. However, compared with tradition ferrograph images from which elaborated debris features can be extracted, current on-line wear debris images only allow to extract features such as quantity, concentration, size and color, which are mainly about statistical characteristics. The detailed morphology information of individual debris that are significant in wear mechanism interpretation, however cannot be reliably extracted so far. This is mainly because the limited image quality which has made the extraction of reliable debris morphology an intractable issue.

In addition, by examining the information on height direction, 3-D debris features have been proved effective in the identification of fatigue chunk, laminar and sliding debris [9]. However, those comprehensive features are not accessible by most existing on-line debris images. A video based debris sensing strategy then was developed for observing wear debris features in multiple views [10]. Experimental result has demonstrated that this method outperforms current 2-D methods by providing volume and height information of wear debris [11]. Nonetheless, the captured debris images often suffer from motion blur due to debris motion when its images are captured. The extracted debris morphology is accordingly significantly affected by the blurry effect.

As can be concluded, the fundamental shortage of current on-line debris image lies in the fact that the image quality is often limited due to contamination and motion blur. Correspondingly, restoration is needed to improve the quality of debris images, allowing the on-line wear debris image to provide more detailed debris features. Image restoration is not a new topic and numerous techniques including inverse filtering, Wiener filtering, least-square filtering and constrained iterative deconvolution methods have been developed [12–16]. However, these techniques cannot be directly applied to address on-line wear debris image as little blur features are known due to the random debris motion. Correspondingly, another estimation strategy called blind deconvolution were proposed to obtain the sharp image and blur features simultaneously [17]. Successful as the restoration is, the iterative computation is relative expensive for on-line wear debris image improvement.

Compared with general blurry image, wear debris image indicates some unique features. First, the blurry effects are mainly generated due to debris motion during the exposure. Furthermore, the information carried is relative lower because of oil contamination and low resolution. Due to this concern, previous research had been carried out to restore the motion-blurred debris image by identifying zeros from the cepstrum of each frame [10]. However, it only works in the scenario with high signal to noise ratio. In on-line monitoring, as the video quality is limited due to the commonly occurred lubrication contamination and resulting in low information content videos, it is difficult or even impossible to identify those periodic zeros. Therefore, a deblurring strategy which allows restoration of debris image with low information content is developed in current work.

The rest of the paper is organized as follows. Related background including wear debris imaging equipment and blurring phenomena of on-line wear debris image are given in Section 2. Section 3 presents the developed method which is composed of four main steps: (1) edge prediction, (2) kernel estimation, (3) primary restoration and (4) image fusion. In Section 4, a 3-D reconstruction experiment is conducted based on real debris profiles to evaluate the performance of the developed method. Finally, a conclusion is given in Section 6.

2. Wear debris sensing equipment and image degradation

In traditional off-line ferrography image analysis, debris are usually manually cleaned and placed on a slide, imaged by a microscope for further examination. However, only single-sided information can be obtained by those approaches. For the purpose of rapidly collecting more comprehensive morphology information, a video based debris imaging system is used [18].

2.1. Video based wear debris analysis

The video based imaging system allows to observe wear debris in different directions by collecting the projected profiles of wear debris from multiple views in images. The system diagram is shown in Fig. 1a.

Lubrication oil containing wear debris is pumped to a micro fluid channel, where a camera is mounted. Due to the viscous drag applied, debris in the fluid channel will rotate and its profiles in multiple views are captured, see in Fig. 1b. Based on those collected profile sequences, three dimensional shape of wear debris can be reconstructed and more detail debris features including volume and thickness can be extracted for wear mechanism interpretation [11].

2.2. Degradation of wear debris image

Video based imaging is capable of acquiring debris information in different views and previous work has been conducted to make it practical in machine monitoring. For instance, debris occlusion can be found when the concentration of debris is large. Debris separation was investigated to extract individual debris from cluster [19,20]. In addition, debris occlusions can also be addressed via a tracking process which allows to identify debris profiles in different poses [21]. However, the performance of current video based debris imaging still needs to be improved as current debris image suffers degradation. It

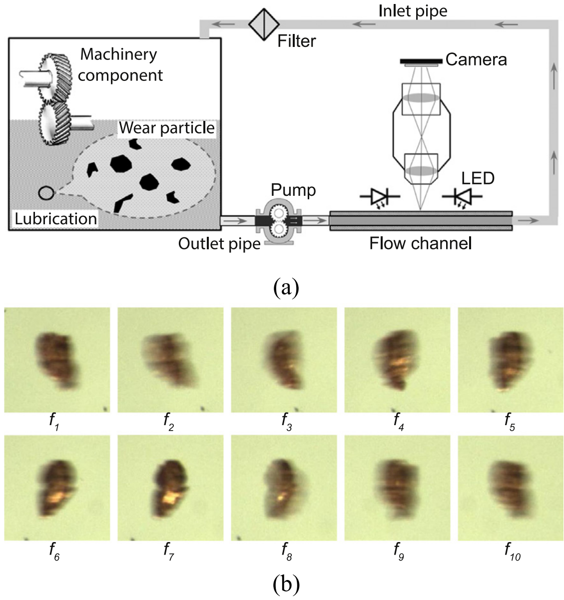

Fig. 1. The imaging equipment and collected debris profile images, (a) the debris imaging system; (b) debris profile sequences.

can be observed from Fig. 1b that the debris profiles are often blurry, especially in the boundary area, making reliable debris shape measurement a challenging task.

Previous research has been conducted to tackle the blurring problem in wear debris analysis [10]. By assuming that wear debris have similar motion speed, zeros in cepstrum are identified and applied to formulate the motion point spread function (PSF). Wiener filtering deconvolution then was applied to obtain the restored debris profile. However, the motion speed of individual wear debris in the flow channel is different due to the dissimilarity of applied viscous drag whose magnitude depends directly on the shape and volume of each debris. In addition, this method only works when the image is captured with sufficient quality. However noise in image is commonly observed due to oil oxidation and contamination, making the identification of zeros from cepstrum a difficult process.

Therefore, a restoration method which could tackle the blurry issue in wear debris image is to be developed. For this purpose, the blurry features of wear debris image is investigated. The motion of wear debris in the flow channel is illustrated in Fig. 2. Once the lubrication oil containing debris is pumped into the flow channel, because of the viscous force applied, those debris will translate and rotate. Motion blur then results from the relative motion between the debris and the camera during the exposure period. On the other hand, as wear debris is a 3-D object, de-focus blur is also possible if the debris is located out of the depth of field. However, this is not the major concern because the distance between the lens and debris is restrained by the fluid channel which thickness is 0.5 mm. In addition, with a controlled flow rate, most of debris will drop to the lower side of the channel due to gravity. As a result, motion blur is the dominating degradation suffered by current video based debris images.

The motion induced blur varies according to the relative motion speed. That means, the image of a point on wear debris will be subjected to more serious blur if the relative motion speed between this point and the camera is higher. As a result, the blurry features of points on boundary areas can be quite different because the motion speed is varying over these areas.

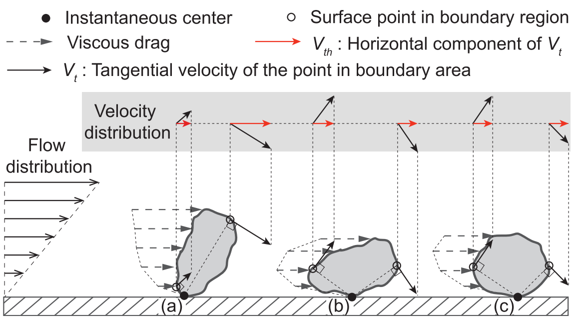

Fig. 2. Viscous drag applied on wear debris and velocity distribution of boundary area.

For the points from a single debris in different posture, shown in Fig. 2a and b, it can be observed from Fig. 2a that the horizontal component of rotation indicate a large difference between the boundary areas on both sides due to different rotation radii. This discrepancy will remit and emerge along with the debris moving, as shown in Fig. 2b. While for spherical debris shown in Fig. 2c, the motion speeds of boundary areas are similar. For small debris which will not contact the flow channel, as the debris motion is a combination of translation and rotation, the motion speed of boundary points will also indicate discrepancy. Therefore, it can be concluded that the relative motion speed of boundary areas on wear debris, which is composed of the translation speed and horizontal component of the rotation speed, are different. This phenomenon will lead to blur of different levels on each side of the debris, this can be observed from the profile sequences shown in Fig. 1b.

Besides the image degradation induced by debris motion that will blur the boundary or even central region of a debris, the quality of wear debris image is often low, namely low informative. This is because lubrication oxidation and contamination are unavoidable, making the illumination from debris surface diffused and refracted by the oil and only partial quantity of intensity is captured by the optical sensor. In addition, the contamination contained in lubrication oil will introduce noise in the captured image. These two process will both reduce the signal to noise ratio of the captured images. As a result, the debris image quality is relative limited compared with those blurry images captured by general cameras which are elaborately configured and their outputs can be well addressed by most of the existing deblurring methods. The blur features of wear debris image can be characterized as:

1. Motion blur is the dominating degradation;
2. The information content is reduced due to insufficient resolution and oil contamination;
3. Due to the spinning and translating of wear debris, the blurry levels of different debris regions are distinct, making the blurring process spatially variant.

Thus, there is the need to conduct the deblurring operation with respect to the specific features of wear debris image. For this purpose, a deblurring method that tackles the varying motion speed of wear debris and low information content is developed.

3. Proposed method

Fig. 3 illustrates the schema of the developed method to restore the blurred on-line wear debris image. Once the raw debris video is captured, particle extraction and tracking are conducted to obtain 2-D profile sequences of a debris that suffers blurring effect. The blurred 2-D images are then processed separately using by the developed restoration method detailed below.

For a blurred profile p_i, the restoration process is carried out in three main steps including edge based PSF estimation, image restoration and profile fusion. Firstly, localized boundary areas are selected to predict the corresponding original sharp boundary, from which two predicted local edges E_1 and E_2 are obtained. Based on the predicted sharp edge and their corresponding observed blurry form, the corresponding localized blur PSFs, also known as blur kernel PSF_1 and PSF_2 are estimated via the Bayesian process. Image restorations of the blurry image are then conducted based on the estimated motion kernels PSF_1 and PSF_2, where different primary deblurred images I_1 and I_2 are obtained. To obtain the final restoration result, the primary restorations I_1 and I_2 are combined by fusing them according to the localized gradient.

3.1. Blurring kernel estimation based on debris edge features

As blurring may significantly affect the shape measurement of wear debris, an operation known as deblurring is to be implemented to remove this limitation. Previous research towards image deblurring often starts by modelling the observed blurry image as a convolution of the underlying sharp image and blur kernel [22], that is

$$I_b(x,y) = \sum_{(n,m)\in\Omega} I_s(x-n, y-m) \times K(n,m) + N(x,y), \tag{1}$$

where I_b is the observed blurry image, K is the PSF defined in patch Ω, and it is also know as blur kernel, I_s is the underlying sharp image, and N denotes additive noise. Given the above model, the objective of image deblurring is to recover the original sharp image I_s from the observed image I_b, which is known as an inverse process called deconvolution.

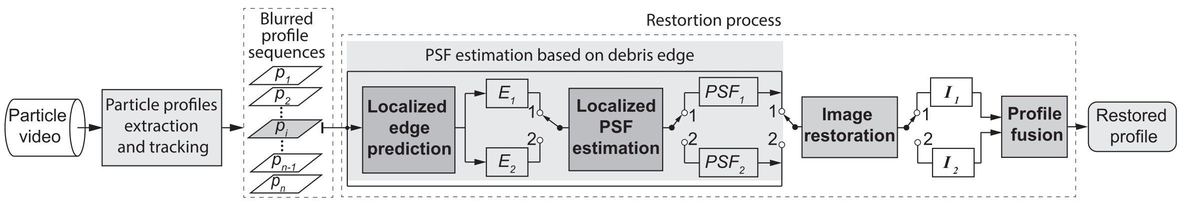

Fig. 3. Block diagram of the restoration process.

Two types of methods called non-blind deblurring and blind deblurring have been proposed over the past decades to tackle this inverse problem [17]. Blind deblurring attempts to obtain the sharp image I_s and PSF K simultaneously from a single blurry image I_b via an iterative process. Although it is regarded as predominant in recent de-blurring related research, the implementation is often complicate, computationally expensive and is not suitable for wear debris image analysis. If the PSF is given, the restoration process is called non-blind deconvolution. This operation is performed with the blurry image I_b given a known blurring PSF, which means that the original sharp image I_s can be obtained immediately via an inverse linear operation. Compared with blind deconvolution, the non-blind strategy is more efficient, and therefore is selected as the deconvolution method in our case, where rapid data interpretation is needed.

To implement non-blind deconvolution, the common procedure is to estimate the blurry PSF first and deconvolution is then performed. A number of studies toward kernel estimation have been conducted including periodic zeros identification and prior statistical assumption [23]. However, the performance of these methods degrade with low signal-to-ratio (SNR) that is commonly observed in wear debris image. Another group of methods seek blur kernel based on edge features, which assumes that edge in the real continuous scene being imaged are step edges of discontinuous intensity [24]. The edge based method is suitable for kernel estimation in wear debris image because debris boundary region is easily identified even in low SNR scenario due to intensity distinctiveness between debris and background. In addition, the estimation of kernel can be handled efficiently compared with blind deconvolution. The following subsections present our method to estimate local blur kernel of debris based on edge features. The process is conducted as two steps: (1) local edge prediction; (2) local kernel estimation.

3.1.1. Local edge prediction

In wear debris image, even the edge is blurred, it is still possible to localized the edge or boundary region because the intensity of debris and background are significantly different. The corresponding local sharp edge can then be predicted from the local blurry boundary area as a process illustrated in Fig. 4. To illustrate the principle with verification, a synthesized debris image is set up to compare the original edge and the predicted edge. In order to simulate the blur process of wear debris, the sharp version of the synthesized debris shown in Fig. 4a is blurred with PSFs of different sizes on the left and right half of the debris, leading to a blurry image shown in Fig. 4b. In particular, the size of PSF on the left half is greater than its counterpart on the right half. This assumption is made based on the fact that the motion features of different surface points are distinct, which can be observed from Fig. 2. Therefore, the blurry level of those two boundary areas in Fig. 4b are distinct, which is consistent with the real blurry images shown in Fig. 1b. To involve the effect of lubricant contamination, Gaussian noise is added to the artificially blurred image.

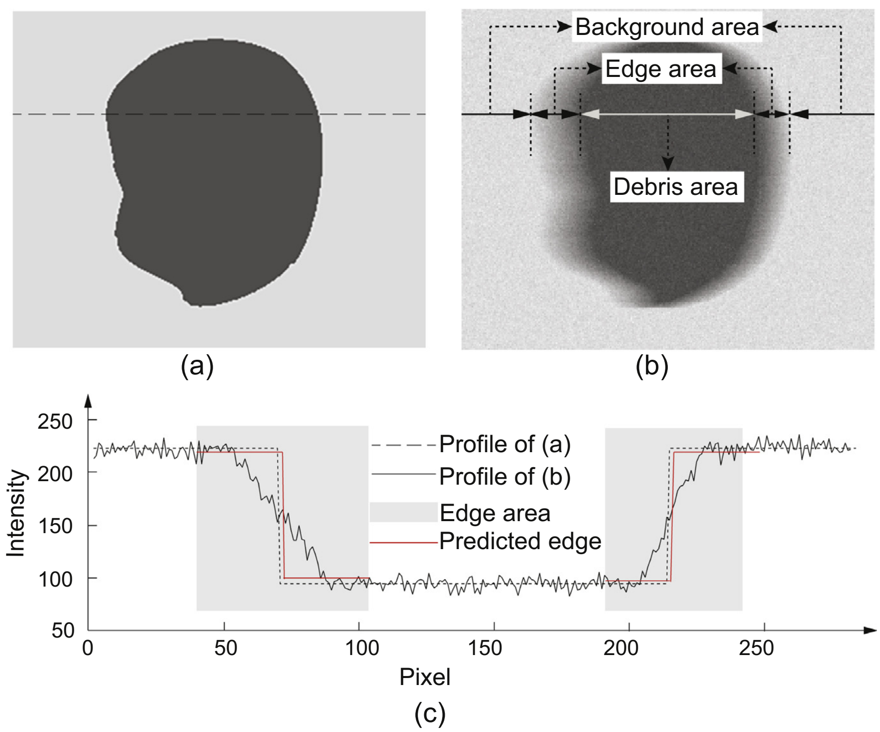

Fig. 4. Edge prediction (a) image with sharp edge (b) synthesized blurry image (c) 1-dimensional cross-sectional view of (a) and (b).

3.1.1.1. Edge model of wear debris. To predict the local edge around the boundary area, the edge model is defined first. Because the debris image intensity distribution is bimodal, a sharp debris image will indicate a step variation in the boundary area due to the distinct intensity change of debris and background. A step edge model is applied to describe wear debris boundary area [25],

$$\bar{I}_{ls}(x) = \begin{cases} \mathcal{I}_b, & x \leqslant x_e \\ \mathcal{I}_d, & x > x_e \end{cases} \quad \bar{I}_{rs}(x) = \begin{cases} \mathcal{I}_b, & x \geqslant x_e \\ \mathcal{I}_d, & x < x_e \end{cases}, \tag{2}$$

where $\bar{I}_{ls}$ and $\bar{I}_{rs}$ are the 1-D step edges on the left and right debris boundary, x_e are the edge location, $\mathcal{I}_b$ and $\mathcal{I}_d$ are background intensity and debris intensity. The position of the local sharp edge is to be predicted by determining the parameters in Eq. (2). The initial values of $\mathcal{I}_b$ and $\mathcal{I}_d$ are determined by averaging the pixel intensity of background and debris area that are away from the edge. The remained task then is to predict the position of x_e and intensity values $\mathcal{I}_b$ and $\mathcal{I}_d$.

3.1.1.2. Debris edge prediction. Based on the assumed step edge $\bar{I}_s$, the unknown parameters in the model can be determined by juxtaposing it with the blurred edge I_b. We assume that the step will locate within each ramp due to the linear properties of motion blur. Then edge prediction is performed by minimizing the difference between the sharp image $\bar{I}_s$ and the blurred edge I_b, which is defined as,

$$E(\bar{x}_e, \bar{\mathcal{I}}_b, \bar{\mathcal{I}}_d) = argmin \sum_{x=1}^{Z} (\bar{I}_s(x) - I_b(x)), \tag{3}$$

where Z is the range of the boundary area, $\bar{x}_e$ is the estimated edge position, $\bar{\mathcal{I}}_b$ and $\bar{\mathcal{I}}_d$ are the estimated intensity of background and debris respectively.

Because the background and debris have distinct intensities, image gradient is used to obtain a coarse estimation on edge location, which is regarded as the initialization of x_e. The intensity value $\mathcal{I}_b$ and $\mathcal{I}_d$ are determined by averaging the intensities of pixels which are lying in the non-edge area. After the parameters are initialized, prediction is accomplished by minimizing the difference defined in Eq. (3) with simplex search [26]. The convergence of this optimization process results in the position of the estimated edge $\bar{x}_e$. Fig. 4c shows the result of edge prediction for 1-D boundary area.

Edge prediction is carried out with one blurred wear debris profile and the result is shown in Fig. 5. As can be observed, based on this prediction model, the sharp edges of different local boundary areas are obtained. It should be noted that due to debris rotation, the central region of debris may suffer from different blurry levels from the boundary region. However, only the edge areas are investigated at this stage. This is because the subsequent PSF estimation will be carried out based on the predicted edge and its blurry boundary, while pixels in the central region provide no useful information for motion features exploration. To reduce the computation, only two local patches on each debris side are investigated. The obtained sharp edges can then be used to estimate the corresponding local PSF.

3.1.2. Localized kernel estimation

As the local sharp edge is predicted, it allows to determine the corresponding kernel within this local boundary area, which indicates the motion features of this region. According to the blur model in Eq. (1), the blurry image I_b can be expressed as a convolution of the sharp image I_s and the blur PSF K. Therefore, in the local boundary area, the formation model can be defined as

$$I_{Lb}(x,y) = \sum_{(n,m)\in\Omega} \bar{I}_s(x-n, y-m) \times K_L(n,m) + N_L(x,y), \tag{4}$$

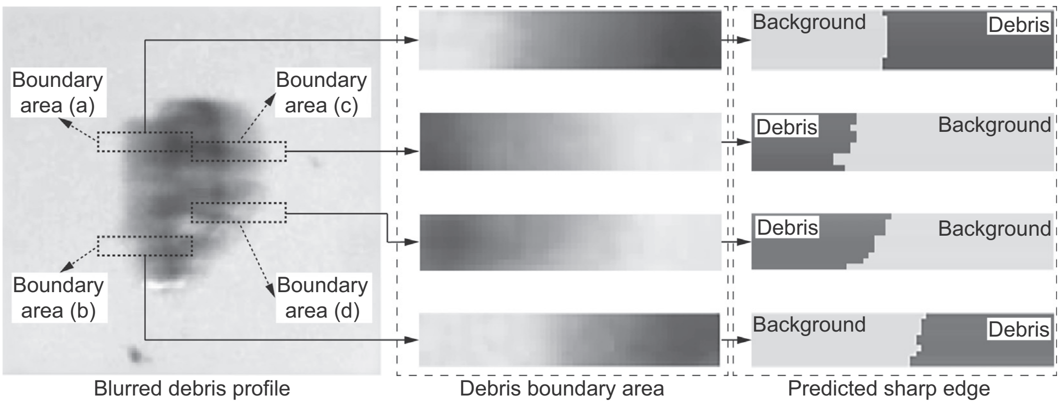

Fig. 5. Edge prediction result for different boundary area.

where I_{Lb} is intensity of pixel in the local blurry boundary area, $\bar{I}_s$ denotes intensity of the predicted sharp edge, K_L is the local PSF and $N_L(x,y)$ is the additive noise which is considered as Gaussian.

To estimate the PSF, a Bayesian framework using maximum a posteriori (MAP) is applied [27]. In particular, the PSF is obtained by seeking the most likely estimation of blur kernel $\overline{K}_L$ given the predicted sharp edge $\bar{I}_s(x,y)$ and its corresponding observed blurry boundary $I_{Lb}(x,y)$. This operation can be expressed with a conditional probability as

$$\overline{K}_L = argmax\ p(K_L|I_{Lb},\bar{I}_s). \tag{5}$$

To calculate the conditional probability, the joint probability of $I_{Lb},\bar{I}_s$ and K_L is determined as

$$p(I_{Lb},\bar{I}_s,K_L) = p(I_{Lb}|\bar{I}_s,K_L)p(\bar{I}_s)p(K_L), \tag{6}$$

where $p(I_{Lb}|\bar{I}_s,K_L)$ denotes the likelihood of blurring process from $\bar{I}_s$ to I_{Lb} via a kernel $K_L, p(K_L)$ is the likelihood of kernel $K_L, p(\bar{I}_s)$ represents the likelihood of the sharp edge $\bar{I}_s$. Similarly,

$$p(I_{Lb},\bar{I}_s,K_L) = p(K_L|I_{Lb},\bar{I}_s)p(I_{Lb})p(\bar{I}_s), \tag{7}$$

where $p(K_L|I_{Lb},\bar{I}_s)$ represents the likelihood of a blur kernel from a blurred image I_{Lb} and its sharp form $\bar{I}_s$.

By equating the right sides of Eqs. (6) and (7), the conditional probability of the kernel K_L based on blurred image I_{Lb} can be obtained as

$$p(K_L|I_{Lb},\bar{I}_s) = \frac{p(I_{Lb}|\bar{I}_s,K_L)p(K_L)}{p(I_{Lb})}. \tag{8}$$

Therefore, the optimal kernel $\overline{K}_L$ can be determined by

$$\overline{K}_L = argmax\ \frac{p(I_{Lb}|I_s,K_L)p(K_L)}{p(I_{Lb})}, \tag{9}$$

As the blurred image I_{Lb} is the observation that is obtained already, $p(I_{Lb})$ is regarded as constant, which means,

$$\overline{K}_L \propto argmax\ p(I_{Lb}|\bar{I}_s,K_L)p(K_L). \tag{10}$$

The imaging noise is assumed as a Gaussian with variance η_1^2 within the blur formation model shown in Eq. (4), which means the probability $p(I_{Lb}|\bar{I}_s,K_L)$ can be written as

$$p(I_{Lb}|\bar{I}_s,K_L) = \frac{1}{(\sqrt{2\pi}\eta_1)^{N_1}}e^{-\frac{\|I_{Lb}-\bar{I}_s\otimes K_L\|^2}{2\eta_1^2}}, \tag{11}$$

where N_1 is the dimension of $I_{Lb}, \otimes$ denotes the convolution operator. For the likelihood term of kernel $p(K_L)$, as the motion of localized area of debris can be regarded as constant motion during the exposure period, the PSF will indicate smoothness. Therefore the gradient of PSF K_L is believed to favour a Gaussian with zero mean and a narrow variance η_2, which therefore can be defined as

$$p(K_L) = \frac{1}{(\sqrt{2\pi}\eta_2)^{N_2}}e^{-\frac{\|\nabla K_L\|^2}{2\eta_2^2}}, \tag{12}$$

where N_2 is the dimension of the PSF. If we define a logarithmic likelihood $L(\cdot) = log(p(\cdot))$, then Eq. (10) can be converted into

$$\overline{K}_L = argmin\ \frac{\|I_{Lb}-\bar{I}_s\otimes K_L\|^2}{\eta_1^2} + \frac{\|\nabla K_L\|^2}{\eta_2^2}. \tag{13}$$

Therefore, the estimated kernel can be determined by minimizing

$$\mathcal{E} = \|I_{Lb}-\bar{I}_s\otimes K_L\|^2 + \lambda\|\nabla K_L\|^2, \tag{14}$$

where $\lambda = \eta_1^2/\eta_2^2$ is regarded as Lagrange multiplier, which represents the penalty regularizing the smoothness of the anticipated kernel $\overline{K}_L$ [26]. The target function defined in Eq. (14) is solved with Newton–Raphson method [28,13].

Accordingly, based on the local blurry image I_{Lb} and the corresponding predicted sharp edge $\bar{I}_s$, a localized motion blur kernel $\overline{K}_L$ can be estimated. Because the motion features can only be assumed invariant in a localized region, the kernel estimation is conducted with blurry image and estimated edge from several truncated regions on the boundary regions. The estimated kernel from those localized regions are shown in Fig. 6. It can be observed that the sizes of the estimated kernels are different, which means that the motion of those boundary areas are indeed different. As mentioned in Section 3.1.1, the motion features of central regions and boundary regions are different due to debris motion. However, as only the motion PSF on the boundary area can be estimated with the predicted edge, we utilize the obtained PSF to represent motion features of its adjacent regions, making the restoration spatially invariant in small patches. This is a common strategy to convert spatial variant deconvolution into spatial invariant deconvolution in multiple local patches [29]. Based on the estimated motion kernels, further deblurring can be performed to obtain the sharp wear debris image.

3.2. Wear debris image restoration with estimated kernels

As the motion PSF is estimated, the deconvolution process can be carried out to recover the original sharp image. For computation efficiency, Wiener filtering is applied to restore the debris image in frequency domain. The process of blurring can be modelled as the convolution in Eq. (4). Its representation in Fourier domain gives

$$\mathcal{I}_b(u,v) = \mathcal{I}_s(u,v) \times \mathcal{K}(u,v) + \mathcal{N}(u,v), \tag{15}$$

where $\mathcal{I}_b(u,v), \mathcal{I}_s(u,v), \mathcal{K}(u,v)$ and $\mathcal{N}(u,v)$ are respectively the transforms of $I_b(x,y), I_s(x,y), \overline{K}(x,y)$ and $N(x,y)$ in frequency domain.

Wiener filter allows to produce a sharp version $\bar{\mathcal{I}}_s$ of the observed $\mathcal{I}_b$ by minimizing the mean square error between the sharp estimation $\bar{\mathcal{I}}_s$ and the ground truth $\mathcal{I}_s$ [12]. The restored result via Wiener filter is given as

$$\bar{\mathcal{I}}_s(u,v) = \mathcal{I}_b(u,v) \times \frac{\mathcal{K}(u,v)}{|\mathcal{K}(u,v)|^2 + \mathcal{S}_n(u,v)/\mathcal{S}_I(u,v)}, \tag{16}$$

where $\mathcal{S}_n(u,v)$ is noise power spectrum, $\mathcal{S}_I(u,v)$ is signal power spectrum. As a result, with a known blur kernel $\mathcal{K}(u,v)$, the sharp particle image $\bar{\mathcal{I}}_s(u,v)$ can be estimated.

As the motion of wear debris in the vertical direction is far less than its motion in horizontal direction, the degradation is dominated by a motion blur process. The motion blur kernel, $K(x,y)$, which is correlated to the debris motion features, is therefore defined as:

$$K(x,y) = \begin{cases} 1/2d, & \text{if } \sqrt{x^2+y^2} < d \\ 0, & otherwise \end{cases}, \tag{17}$$

where d is the size of estimated localized kernels. Based on defined kernel $K(x,y)$, restoration $\bar{\mathcal{I}}_b(u,v)$ is obtained according to Eq. (16).

Since the motion features are distinctive on left and right sides of wear debris, two restorations are implemented based on two different motion kernels estimated from the left and right sides of debris, shown in Fig. 7b and d. The restorations results are given in Fig. 7c and e.

After restoration, the contrast of wear debris profile from background is improved as part of the boundary area is sharper than the original one. However, each restoration result still contains under-restored regions. As can be observed from Fig. 7, the restoration result shown in Fig. 7c indicates a sharper boundary on the left side than its corresponding area in Fig. 7e, and vice versa. This is because the PSF applied in each deconvolution is estimated from one side of debris, which means that it can only cope with the restoration of wear debris near the corresponding boundary area, while the rest of blurred area cannot be well recovered. This is also the shortage of most existing deblurring techniques that restore the degraded image with one single invariant PSF. In order to maintain the sharp area and remove the undesired part, a fusion process is implemented to obtain the final debris image after the primary restoration results are obtained.

3.3. Debris profiles fusion from multiple deblurring images

For the purpose of merely maintain the desired restoration area, a fusion method is introduced to obtain the final restoration result. The local sharpness of restoration results are firstly evaluated to roughly determine the desired area. Image fusion then is implemented to obtain the ultimate restoration.

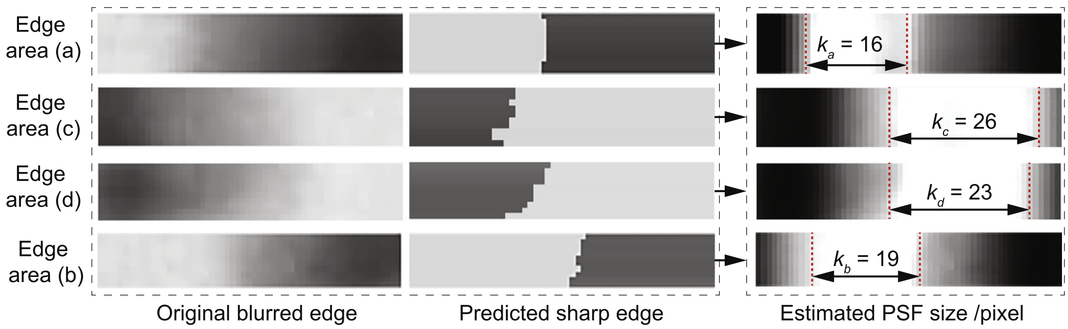

Fig. 6. Estimated kernel for different boundary areas.

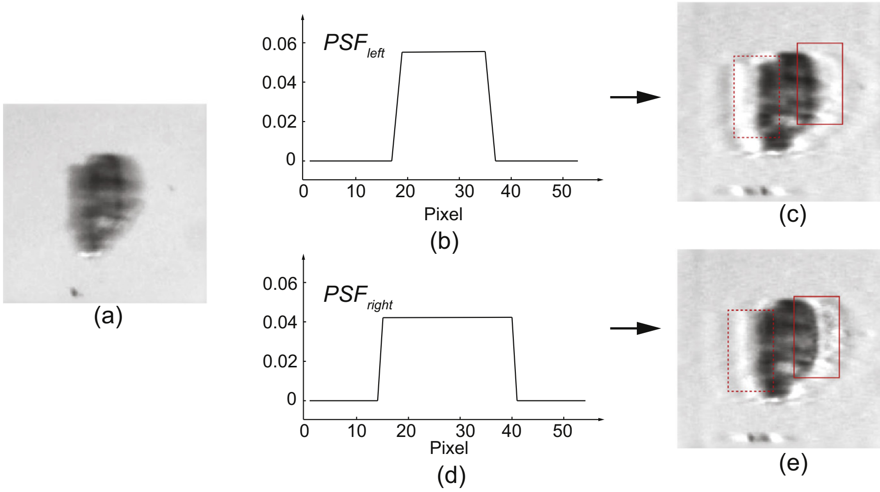

Fig. 7. Restoration result with different localized point spread function.

3.3.1. Sharpness evaluation

The sharpness of an image can be quantified as the intensity distinctiveness in the local area around each pixel. A metric called spatial frequency, $SF(x,y)$, has been developed as an effective indicator to reflect the clarity of the image [30]. For instance, when the blur around one pixel increased, its spatial frequency reduces correspondingly. For a specific pixel $I(x,y)$, this indicator is defined as

$$SF(x,y) = \sqrt{RF(x,y)^2 + CF(x,y)^2}, \tag{18}$$

where $RF(x,y)$ and $CF(x,y)$ are the row frequency and column frequency, which are determined as:

$$RF(x,y) = \sqrt{\frac{1}{M \times N}\sum_{m=1}^{M}\sum_{n=1}^{N}[I(x-m,y-n) - I(x-m,y-n+1)]^2}, \tag{19}$$

and

$$CF(x,y) = \sqrt{\frac{1}{M \times N}\sum_{m=1}^{M}\sum_{n=1}^{N}[I(x-m,y-n) - I(x-m+1,y-n)]^2}, \tag{20}$$

in which M and N are the size of a local image patch centered at position (x,y). With this indicator, the sharpness of individual pixel could be quantified, allowing the identification and extraction of sharper region to fuse the final restoration result that is illustrate as following.

3.3.2. Profiles fusion based on localized sharpness

The final restoration result is obtained by combining two restored debris profiles according to the local sharpness. The fusion process is implemented in the following steps with the two restorations shown in Fig. 7c and e. The detailed process are demonstrated as following with key results shown in Fig. 8.

Step 1: For result comparison, the preliminary restorations obtained from Section 3.2 are listed as Fig. 8a and b. Spatial frequency SF_1 and SF_2 for two primary restorations given in Fig. 8a and b are calculated according to Eq. (20). The local image patch used is a 5×5 window ($M = N = 5$). The spatial frequency of the two primary restoration are shown in Fig. 8c and d. As can be observed, compared with the background, the boundary area indicates greater sharpness value.

Step 2: Focus map construction. The focus map is constructed by comparing the spatial frequency values SF_1 and SF_2 at each pixel (x,y). As the pixel with higher spatial frequency value represent sharper image, it is regarded as the focused candidate. Based on this concept, the focus map I_m is defined as

$$I_m(x,y) = \begin{cases} 1, & SF_1(x,y) > SF_2(x,y) \\ 0, & otherwise \end{cases}. \tag{21}$$

With Eq. (21), the pixel with higher sharpness will be labeled as 1 while the rest will be labeled as 0, the focus map of two input images are then built, shown in Fig. 8e and f. It can be observed that the focus map can indicate which pixel is sharper out of two images at (x,y).

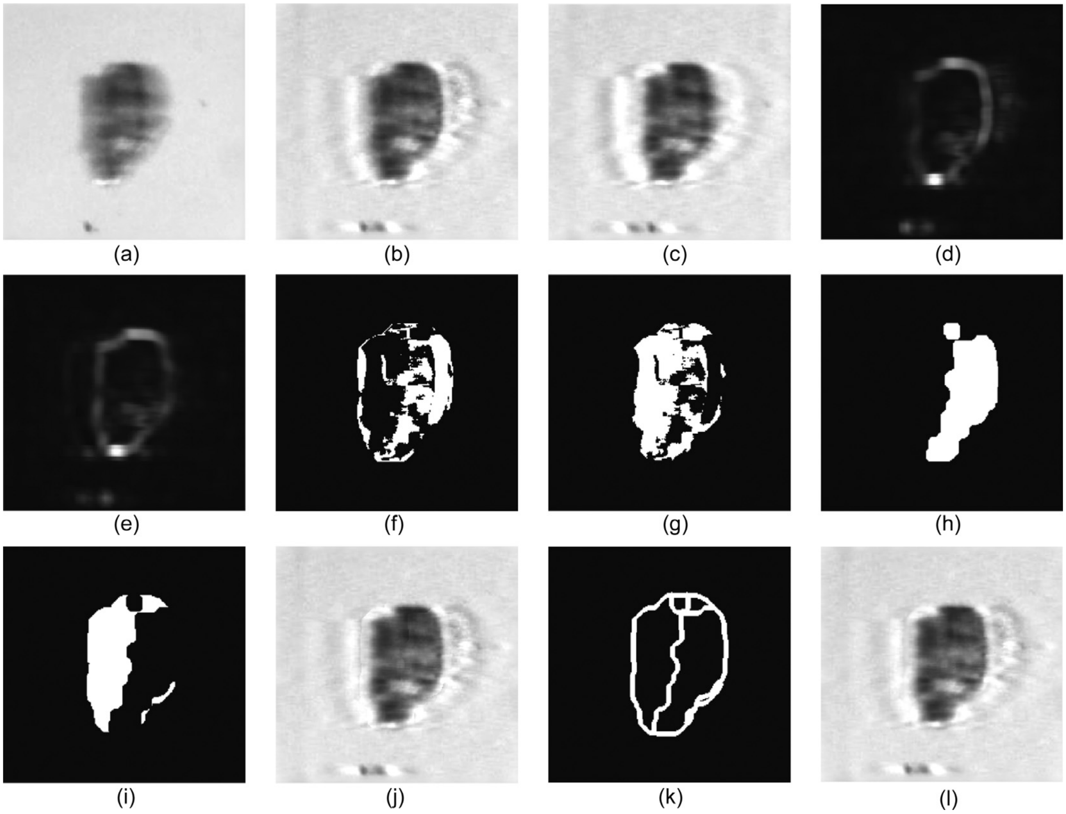

Fig. 8. Image fusion based on the primary restored images, (a) blurry profile; (b) Restoration result based on PSF estimated from right debris boundary; (c) Restoration result based on PSF estimated from left debris boundary; (d) spatial frequency of (b); (e) spatial frequency of (c); (f) focus map of (b); (g) focus map of (c); (h) filtered version of (f); (i) filtered version of (g); (j) preliminary fusion result; (k) discontinuity area of (j); (l) final fusion result.

However, there are still thin protrusions, narrow breaks and small holes remained in the map shown in Fig. 8e and f, while the focus regions are usually continuous. To rectify those defects, morphological opening and closing, implemented by combining dilation and erosion are conducted. With a defined structure element E (disk, radius = 5), the opening operation, denoted as $I_m \circ E$, is a erosion followed by a dilation, which can remove thin protrusion. The closing operation, denoted as $I_m \bullet E$, is a dilation followed by erosion, which can fill the noncontinuous break and hole. After morphological filtering, a smoothed focus map $\bar{I}_m(x, y)$ is obtained, shown in Fig. 8g and h.

Step 3: Image fusion. the updated focus map indicates whether a pixel is sharp or not. As only the sharper pixel will be maintained, a the fusion process followed to achieve this objective. The fused image is constructed as

$$I_f(x, y) = \begin{cases} I_{r1}(x, y), & \bar{I}_m(x, y) = 1 \\ I_{r2}(x, y), & otherwise \end{cases}, \tag{22}$$

which is displayed in Fig. 8 i. However, artefacts can be observed at the boundary area of focal map listed in Fig. 8. Median filter then is applied to smooth the discontinuity, resulting in the ultimate restoration result, shown in Fig. 8k.

The above three steps allow to formulate the final restoration result based on two preliminary deblurred debris profiles that contains under-restored area inside. Those under-restored areas will be removed and only the sharper part of the deblurred profiles would be maintained in the final result. As can be observed, compared with the primary restoration, the fusion result retains sharper region in the primary restoration output.

4. Evaluation of the developed method

The developed restoration strategy enables to obtain the debris contour with higher confidence, which will improve the accuracy of debris identification. To evaluate the performance of the developed method, related methods are compared in this section. In addition, experiments upon different debris images are carried out to demonstrate its capability in different scenarios.

4.1. Evaluation of the method with respect to edge prediction and image restoration

The developed method consists of edge prediction, kernel estimation and fusion based image deconvolution. However, related approaches for edge extraction and image deconvolution have also been developed to address similar issues. To demonstrate the performance of the proposed method, it is compared with those well-known techniques including edge extraction and image deconvolution.

In this work, debris edge is predicted with a localized step model. However, the localized edge can also be estimated by Canny and Sobel operator that are commonly applied in edge detection [31,32]. We implemented those two methods upon the blurred debris image shown in Fig. 5 and the results are given in Fig. 9.

As can be observed, the edge extracted by Canny detector is very sensitive to detail features such as texture and noise. As shown in Fig. 9a, redundant edges are extracted compared with the result presented in Fig. 5. The result obtained via Sobel detector proves its higher robustness in details, but still suffers from multiple edges in the localized boundary regions, shown in Fig. 9b. As a single edge is required to estimate the motion kernel size, those two edge detectors cannot be used to predict the localized edge of wear debris.

In the proposed method, the sharp debris image is obtained by fusing the deblurring results from Wiener filtering based deconvolution. However, deblurring strategies such as Lucy-Richardson and blind deconvolution can also be used to restore blurring image [16,17]. We have implemented image deblurring with those three methods and the results are shown in Fig. 10.

Compared with the result of our method, Lucy-Richardson and blind deconvlution can achieve comparable restoration performance, as shown in Fig. 10b and c. Nonetheless, our method is preferred due to its computation efficiency. The computation cost of the aforementioned methods are detailed in Table 1. The size of the processed image is 118×114. The code is programmed in MATLAB on a personal computer with Intel Core i5-4750 CPU and 16 GB RAM.

As listed in the Table 1, three steps including PSF estimation, image deconvolution and image fusion are required to restore the blurring image. For non-blind restoration strategy including our method and Lucy-Richardson deconvolution, the PSF needs to be determined before image deconvolution can be implemented. However, the Lucy-Richardson deconvolution incurs higher total computation than the developed method. This is because it is implemented as an iterative process. For blind deconvolution, although the PSF is usually not required for the deconvolution process, the deconvolution step asks for much higher computation than the other two methods. In addition, the blind deconvolution process is highly dependent on the size of the initialized kernel, as shown in Fig. 10d, e and f. As a result, although those three methods can be used in the deconvolution step and achieve comparable final results, the Wiener filtering approach is most preferred because this method is developed to process on-line wear debris image where computation cost is a major concern.

4.2. Evaluation of the method with respect to 3-D debris morphology measurement

The motivation of this research is to improve the accuracy of the extracted debris profile that will significantly influence the ultimate measurement of debris shape such as size and morphology. In particular, 3-D features including thickness and volume will also be affected. All those features will directly impact the wear debris identification and classification. To evaluate the performance of the developed method, restoration of blurred debris profiles is conducted firstly, then 3-D shape measurements follows based on the restored debris profiles.

Fig. 11 illustrates the restoration result of the multiple view profiles shown in Fig. 1b. In particular, those blurry profiles are firstly converted into their grayscale forms for comparison, as depicted in Fig. 11a. Due to the blurry effect, those

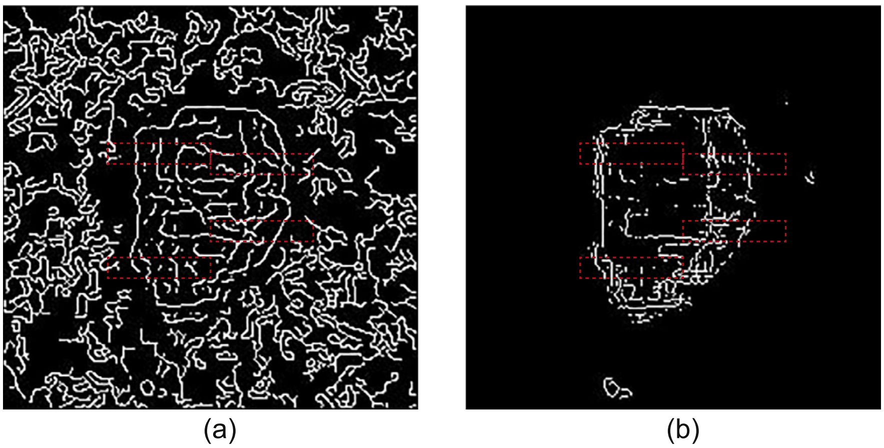

Fig. 9. Debris edge extraction with Canny and Sobel detector, (a) result of Canny detector, (b) result of Sobel detector.

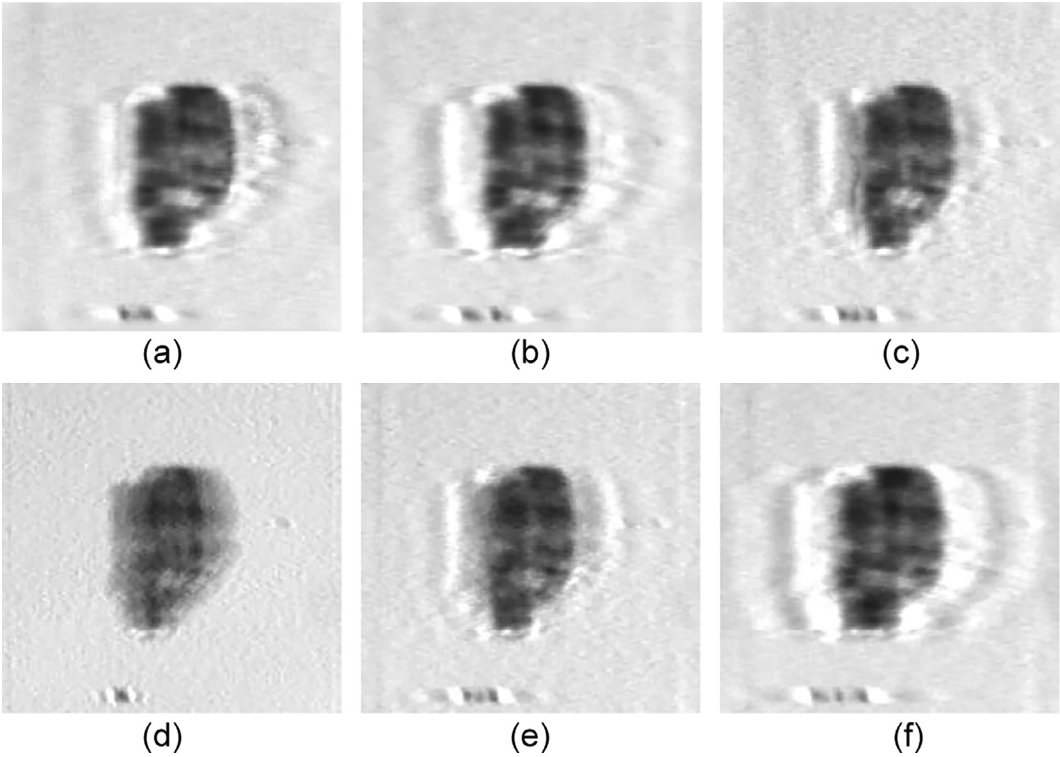

Fig. 10. Deblurring with different deconvolution approaches, (a) restoration result of our method, (b) fusion result of Lucy-Richardson deconvolution, (c) fusion result of blind deconvolution, (d) blind deconvolution with initial kernel size of 10, (e) blind deconvolution with initial kernel size of 20, (f) blind deconvolution with initial kernel size of 40.

Table 1
Computation cost of three restoration methods.

Step	Restoration method		
	Our method	Lucy-Richardson	Blind deconvolution
PSF estimation (/s)	0.0536	0.0521	0.0527
Image deconvolution (/s)	0.0181	0.1115	0.1647
Image fusion (/s)	0.2152	0.1968	0.2101
Total time (/s)	0.2869	0.3604	0.4275

extracted contours do not accurately indicate the actual 2-D debris silhouettes. With the developed method, restored profiles are obtained and given in Fig. 11b. As can be observed, those blurry profiles are sharpened by the developed method to remove the degradation effect on contour extraction. The ultimate recovered debris profiles are extracted by removing the artifacts emerged in the background area, as shown in Fig. 11c. It should be noted that there are some bright regions in the restored debris profile, as shown in Fig. 11b and c. This phenomenon is usually induced by two sources. Firstly, as the product of friction, some regions on debris can be very smooth that may reflect the illumination light into the camera and then produce the bright region. Those white regions in debris image can also be observed in Ferrography images [33]. In addition, the Wiener filtering deconvolution may also cause over saturation due to the operation of matrix inversion. However, as the presented method is to improve the 3-D debris measurement, those bright regions are still tolerable for debris shape investigation. The updated contours extracted from the recovered profiles then can be applied for 3-D debris measurement.

Fig. 11 demonstrates that the developed method is capable of recovering profiles of individual debris in different views that indicate different blur level. To further evaluate the method, restoration is also carried upon blurry profiles from different wear debris in various illumination condition, shown in Fig. 12.

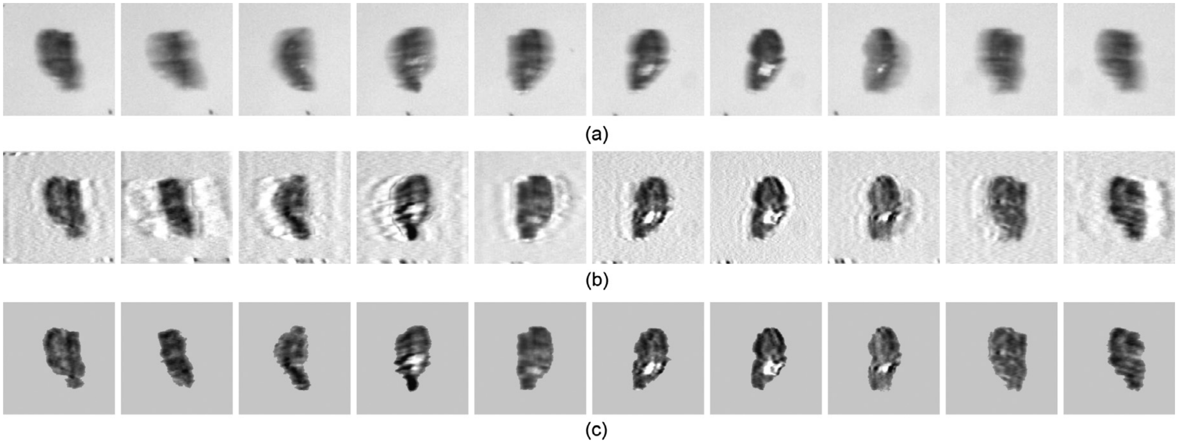

Fig. 11. Improvement of the restoration on debris shape measurement, (a) blurry profile sequences, (b) restored profile sequences, (c) extracted profile sequences.

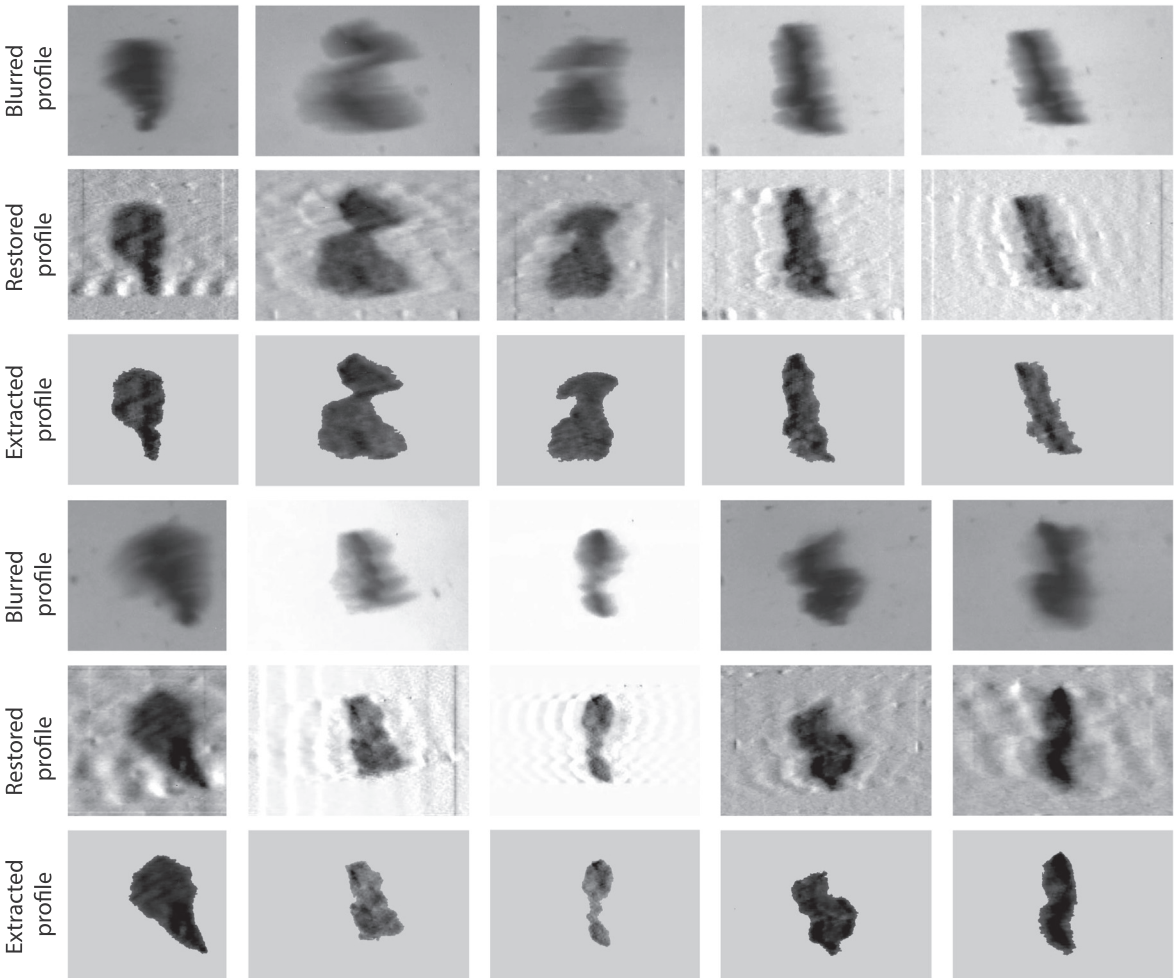

Fig. 12. Restoration of blurry profiles from different wear debris.

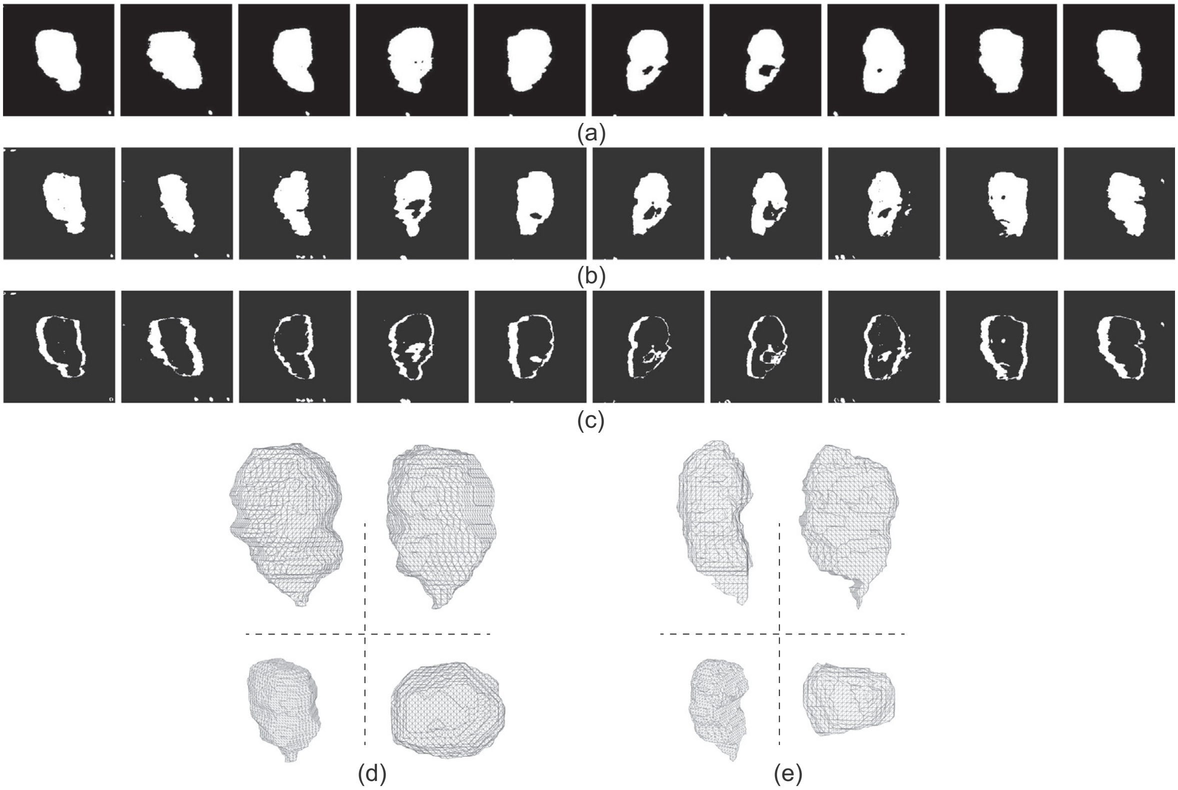

Fig. 13. 3-D measurements based on blurred and restored profiles, (a) contours of the blurry profiles, (b) contours of the restored profiles, (c) differences between the blurry contours and the restored contours, (d) 3-D reconstruction with blurry contours, (e) 3-D reconstruction with restored contours.

Table 2
Detail features of 3-D reconstructed debris in Fig. 13d and e.

Debris	Debris features				
	L (μm)	W (μm)	H (μm)	*HAR*	V ($\times 10^3$ μm^3)
Fig. 11f	36	28	26	1.38	12.67
Fig. 11g	35	27	18	1.94	7.39
Difference (%)	2.78	3.57	30.77	40.58	41.67

As can be observed, most of the blurry profiles can be restored significantly with respect to debris contour. However, it should be noted the profiles in brighter illumination condition will arise less artifacts in the restoration, which is due to the fact that brighter image indicate higher SNR.

It can be concluded that the developed method is able to restore blurred debris profiles under different motion and illumination conditions. Compared with the contours of the blurry profile, the contours extracted from restored images indicate apparent differences, shown in Fig. 11. Considering the nature of shape-from-silhouette, those 2-D dissimilarities will accumulate and eventually result in greater error in 3-D debris features. To demonstrate this discrepancy, 3-D reconstructions are carried out based on the original blurry contours and the recovered contours respectively, which is illustrated in Fig. 13.

To implement 3-D reconstruction, the blurry and restored debris profiles listed in Fig. 11 are converted into binary forms, as shown in Fig. 13a and b. The contour differences, shown in Fig. 13c will result in a diversity in shape measurement. 3-D reconstruction based on the blurry and restored profiles are given in Fig. 13d and e, which morphological details are listed in Table 2. Indicators L, W, H represent the length, width and thickness of a debris respectively. V denotes the volume. Height Aspect Ratio (HAR) is the ratio of the maximum dimension to minimum dimension, which is also known as thickness. As can be observed, from the reconstruction result, those two 3-D debris suggest markedly morphological distinction.

By comparing the 3-D shape from the recovered profiles and blurry profiles, it is shown that the blurring effect are reduced, making the contour extraction more accurate. As a result, debris features especially for thickness and volume can be modified significantly with the developed restoration process.

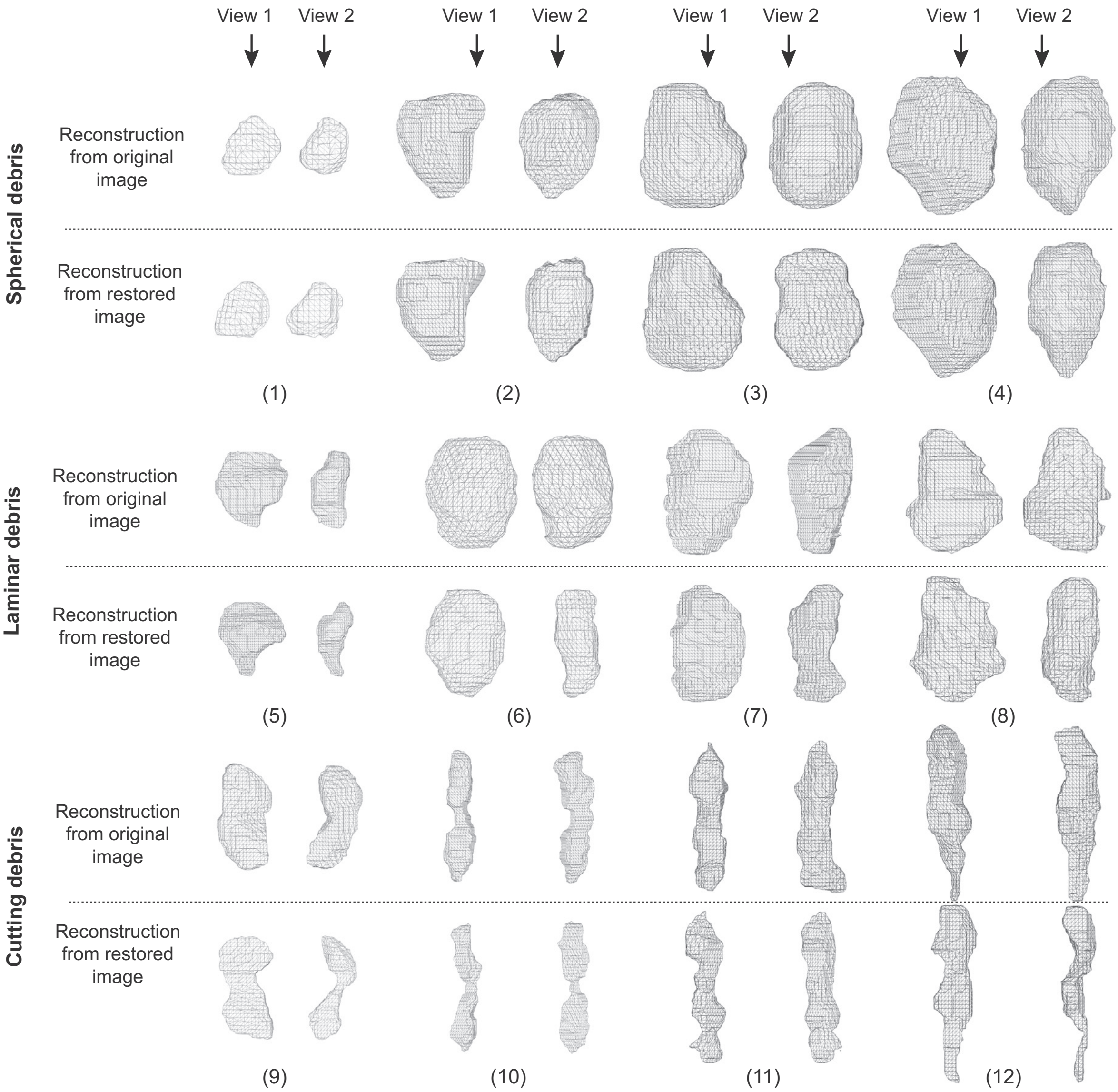

Fig. 14. 3-D debris reconstructed from original blurry images and restored images.

To further evaluate this method in debris shape description, 3-D measurements were implemented with three types of wear debris, whose video was collected from gearbox lubrication oil. In the experiment, the initial 3-D debris shape measurement was firstly carried out based on blurry debris profiles. Those blurry profiles then were recovered by the developed deblurring method to remove the blurry effect. The 3-D shape measurement was repeated based on those recovered debris profiles. The 3-D reconstructed results are illustrated in Fig. 14.

The morphological details of debris shown in Fig. 14 is listed in Table 3. The updated 3-D debris shape measurements, denoted as $\mathcal{R}$ were compared with the initial 3-D debris shape measurements, denoted as $\mathcal{O}$, to demonstrate the performance of the deblurring operation.

As can be observed from the comparison result, debris shape measurement from the blurry profile and the restored profile indicate significant difference. For instance, debris 6 was originally classified as spherical debris based on its *HAR* value that is close to 1. However, because the thickness features were ameliorated via the restoration operation, the *HAR* value increase dramatically, making them to indicate laminar features. Similar features can also be observed from debris $5, 7, 12$ and 8. Due to the improvement of thickness features, cutting features will also be enhanced by recovering the blurred profiles. In addition, as the debris shape is more reliably described, the estimation of material loss that is related to debris volume, will also be obtained with higher confidence.

Table 3
Difference of initial and updated debris morphology in Fig. 14.

Debris		Debris features									
		L (μm)		W (μm)		H (μm)		HAR		V ($\times 10^3$ μm^3)	
Type	ID	$\mathcal{O}$	$\mathcal{R}$	$\mathcal{O}$	$\mathcal{R}$	$\mathcal{O}$	$\mathcal{R}$	$\mathcal{O}$	$\mathcal{R}$	$\mathcal{O}$	$\mathcal{R}$
Sphere	(1)	25	24	23	19	21	18	1.19	1.33	5.75	3.87
	(2)	45	43	36	34	32	28	1.41	1.54	24.80	19.57
	(3)	52	50	47	44	43	39	1.21	1.28	47.77	38.82
	(4)	60	56	51	47	40	32	1.50	1.75	58.57	40.29
Laminar	(5)	34	32	29	24	19	13	1.79	2.46	8.87	4.61
	(6)	46	45	39	34	33	16	1.39	2.81	27.28	10.98
	(7)	53	50	35	31	28	22	1.89	2.27	24.05	15.70
	(8)	53	53	45	45	40	25	1.33	2.12	44.58	27.73
Cutting	(9)	46	43	20	20	15	14	3.07	3.07	5.31	4.18
	(10)	57	55	15	13	14	10	4.07	5.50	6.02	3.81
	(11)	62	62	17	13	15	12	4.13	5.17	7.19	4.46
	(12)	75	76	18	10	16	8	4.69	9.50	10.59	5.98

This method is able to mitigate motion blur degradation that is common in on-line wear debris image. It can improve the robustness of video-based debris imaging in industrial application. In addition, the rectification of debris profile will influence the further wear mechanism interpretation as well because of the modified debris features. Based on the blurred features, the debris is similar as a sphere debris according to its *HAR* value. While after the restoration, the *HAR* varies dramatically enabling this debris to indicate laminar and cutting features.

5. More discussion

This approach differs from previous ones in several ways. Firstly, multiple motion PSFs are utilized to restore the blurred debris profiles that suffer distinct motion blur in different regions. Second, a fusion process is implemented to remove the undesired restoration and maintain the sharp regions. It enables describing the morphological information of debris with higher confidence.

With the improved 2-D profiles, debris contours can be described more accurately, allowing the morphological features defined in off-line debris image to be applicable in on-line analysis. In addition, 3-D debris shape can be measured more elaborately with the improved 2-D contours. Debris in fatigue chunk, laminar and spherical then can be classified, enabling interpretation of more detail wear mechanism. Furthermore, the 3-D features such as debris volume can be used to estimate material loss from machinery components, which is regarded as an indicator of wear rate.

However, future works are still needed to make it more practical and robust. Although motion blur is the major issue addressed in this work, de-focus blur can also be observed when the dimension of debris is large. However, most existing methods are developed to tackle specific blur degradation. The presented method therefore is needed to be improved as a comprehensive strategy that can restore debris image in various degradation in the future. On the other hand, the developed method can improve the boundary information that is important in shape description. However, the surface information still cannot be restored with sufficient confidence. Future research is still needed to recover more detail debris surface information such as texture.

6. Conclusion

In this work, a fusion based deblurring strategy is developed for the restoration of wear debris image with low information content. Debris edge features are adopted to predict the local motion kernel that is difficult to be estimated directly by other methods. Based on the fact that debris blur is a spatially variant process, Wiener filtering is employed to obtain the deblurred images with different local kernels. To maintain the desired sharp area and discard parts containing residual blur, a fusion process is implemented to extract the optimal restoration effect. The experiment result demonstrates that this method is capable of restoring debris image captured under lubrication contamination and oxidation. With the debris profile restored, shape measurement and morphology analysis of debris are improved, making the video based debris monitoring more robust and practical.

Acknowledgement

The presented research was supported by the China Scholarship Council (Grant No. 201506280014).

References

[1] A.K. Jardine, D. Lin, D. Banjevic, A review on machinery diagnostics and prognostics implementing condition-based maintenance, Mech. Syst. Signal Process. 20 (7) (2006) 1483–1510.
[2] W. Hong, S. Wang, H. Liu, M.M. Tomovic, Z. Chao, A hybrid method based on band pass filter and correlation algorithm to improve debris sensor capacity, Mech. Syst. Signal Process. 82 (2017) 1–12.
[3] X. Zhu, L. Du, J. Zhe, A 3 × 3 wear debris sensor array for real time lubricant oil conditioning monitoring using synchronized sampling, Mech. Syst. Signal Process. 83 (2017) 296–304.
[4] J. Wang, J. Bi, L. Wang, X. Wang, A non-reference evaluation method for edge detection of wear particles in ferrograph images, Mech. Syst. Signal Process. 100 (2018) 863–876.
[5] W. Yuan, K. Chin, M. Hua, G. Dong, C. Wang, Shape classification of wear particles by image boundary analysis using machine learning algorithms, Mech. Syst. Signal Process. 72 (2016) 346–358.
[6] B. Roylance, Ferrographythen and now, Tribol. Int. 38 (10) (2005) 857–862.
[7] T. Wu, H. Wu, Y. Du, Z. Peng, Progress and trend of sensor technology for on-line oil monitoring, Sci. China Technol. Sci. 56 (12) (2013) 2914–2926.
[8] T. Wu, J. Mao, J. Wang, J. Wu, Y. Xie, A new on-line visual ferrograph, Tribol. Trans. 52 (5) (2009) 623–631.
[9] Z. Peng, T. Kirk, Z. Xu, The development of three-dimensional imaging techniques of wear particle analysis, Wear 203 (1997) 418–424.
[10] Y. Peng, T. Wu, S. Wang, N. Kwok, Z. Peng, Motion-blurred particle image restoration for on-line wear monitoring, Sensors 15 (4) (2015) 8173–8191.
[11] H. Wu, N.M. Kwok, S. Liu, T. Wu, Z. Peng, A prototype of on-line extraction and three-dimensional characterisation of wear particle features from video sequence, Wear 368 (2016) 314–325.
[12] A. Jain, S. Ranganath, Application of two dimensional spectral estimation in image restoration, in: Acoustics, IEEE International Conference on ICASSP'81 Speech, and Signal Processing, vol. 6, IEEE, 1981, pp. 1113–1116.
[13] B.R. Hunt, The application of constrained least squares estimation to image restoration by digital computer, IEEE Trans. Comput. 100 (9) (1973) 805–812.
[14] A. Aboutalib, L. Silverman, Restoration of motion degraded images, IEEE Trans. Circ. Syst. 22 (3) (1975) 278–286.
[15] J. Biemond, R.L. Lagendijk, R.M. Mersereau, Iterative methods for image deblurring, Proc. IEEE 78 (5) (1990) 856–883.
[16] W.H. Richardson, Bayesian-based iterative method of image restoration, JOSA 62 (1) (1972) 55–59.
[17] P. Campisi, K. Egiazarian, Blind Image Deconvolution: Theory and Applications, CRC press, 2016.
[18] Y. Peng, T. Wu, S. Wang, Y. Du, N. Kwok, Z. Peng, A microfluidic device for three-dimensional wear debris imaging in online condition monitoring, Proc. Inst. Mech. Eng., Part J: J. Eng. Tribol. 231 (8) (2017) 965–974.
[19] H. Wu, T. Wu, Y. Peng, Z. Peng, Watershed-based morphological separation of wear debris chains for on-line ferrograph analysis, Tribol. Lett. 53 (2) (2014) 411–420.
[20] J. Wang, P. Yao, W. Liu, X. Wang, A hybrid method for the segmentation of a ferrograph image using marker-controlled watershed and grey clustering, Tribol. Trans. 59 (3) (2016) 513–521.
[21] A. Yilmaz, X. Li, M. Shah, Contour-based object tracking with occlusion handling in video acquired using mobile cameras, IEEE Trans. Pattern Anal. Mach. Intell. 26 (11) (2004) 1531–1536.
[22] D. Kundur, D. Hatzinakos, Blind image deconvolution, IEEE Signal Process. Magaz. 13 (3) (1996) 43–64.
[23] H. Ji, C. Liu, Motion blur identification from image gradients, in: Computer Vision and Pattern Recognition, 2008. CVPR 2008. IEEE Conference on, IEEE, 2008, pp. 1–8.
[24] L. Sun, S. Cho, J. Wang, J. Hays, Edge-based blur kernel estimation using patch priors, in: Computational Photography (ICCP), 2013 IEEE International Conference on, IEEE, 2013, pp. 1–8.
[25] N. Joshi, R. Szeliski, D. J. Kriegman, Psf estimation using sharp edge prediction, in: Computer Vision and Pattern Recognition, 2008. CVPR 2008. IEEE Conference on, IEEE, 2008, pp. 1–8.
[26] S.S. Rao, S.S. Rao, Engineering Optimization: Theory and Practice, John Wiley & Sons, 2009.
[27] R. Fergus, B. Singh, A. Hertzmann, S. T. Roweis, W. T. Freeman, Removing camera shake from a single photograph, in: ACM Transactions on Graphics (TOG), Vol. 25, ACM, 2006, pp. 787–794.
[28] B.R. Masters, R.C. Gonzalez, R. Woods, Digital image processing, J. Biomed. Opt. 14 (2) (2009) 029901.
[29] S. H. Chan, T. Q. Nguyen, Single image spatially variant out-of-focus blur removal, in: Image Processing (ICIP), 2011 18th IEEE International Conference on, IEEE, 2011, pp. 677–680.
[30] M.A. Rahman, S. Liu, C.Y. Wong, S. C.-F. Lin, S. Liu, N.M. Kwok, Multi-focal image fusion using degree of focus and fuzzy logic, Digital Signal Process. 60 (2017) 1–19.
[31] N. Kanopoulos, N. Vasanthavada, R.L. Baker, Design of an image edge detection filter using the sobel operator, IEEE J. Solid-State Circ. 23 (2) (1988) 358–367.
[32] L. Ding, A. Goshtasby, On the canny edge detector, Pattern Recogn. 34 (3) (2001) 721–725.
[33] S. Raadnui, Wear particle analysisutilization of quantitative computer image analysis: a review, Tribol. Int. 38 (10) (2005) 871–878.